Journal of
Mechanics of
Materials and Structures

THERMAL STRESS ANALYSIS OF FUNCTIONALLY GRADED COMPOSITES WITH TEMPERATURE-DEPENDENT MATERIAL PROPERTIES

H. K. Ching and J. K. Chen

Volume 2, Nº 4 April 2007

mathematical sciences publishers

JOURNAL OF MECHANICS OF MATERIALS AND STRUCTURES
Vol. 2, No. 4, 2007

THERMAL STRESS ANALYSIS OF FUNCTIONALLY GRADED COMPOSITES WITH TEMPERATURE-DEPENDENT MATERIAL PROPERTIES

H. K. CHING AND J. K. CHEN

Thermomechanical deformation of a functionally graded composite (FGC) in elevated temperature environments is investigated by the meshless local Petrov–Galerkin method. The FGC is modeled as a 2-D linearly elastic solid which consists of ceramic ZrO_2 and alloy Ti-6Al-4V with the volume fraction varying along a predefined direction. Unlike most investigations performed so far, temperature-dependent thermophysical and thermomechanical properties are considered for both constituents in this work. The effective material properties of the FGC are evaluated with the micromechanical models. An FGC hollow cylinder under an internal temperature change is first studied; the numerical results agree very well with those computed by the finite element method. The parametric studies with respect to different profiles of graded FGCs are performed for a clamped-clamped thick beam and a square plate with a central hole, respectively. It is found that inclusion of temperature dependence for the material properties has a great impact on thermomechanical response prediction for FGCs in elevated temperature environments.

1. Introduction

Among functionally graded composites (FGCs), those made from ceramics and metals have received considerable attention in the structural ceramic applications, including gas turbines, hot engine components, packaging encapsulants, thermoelectric generators, and human implants, to name a few. The reasons for receiving such a great attention are two-fold: (1) the ceramic phase provides corrosion, wear and erosion resistance, possesses higher compressive strength, and can protect the structural components from severe thermal or biological environments; (2) a microscopically heterogeneous FGC engineered to a continuous spatial variation by grading the volume fraction of the material constituents can reduce interfacial stresses in a coated structure, minimize stress concentration or intensity factors, and attenuate stress waves, etc.

Numerous theoretical studies have been conducted for investigating linearly elastic thermomechanical response of FGCs. Although analytical approaches provide closed-form solutions [Zimmerman and Lutz 1999; Tarn 2001; Sankar and Tzeng 2002; Vel and Batra 2002; 2003; Ootao and Tanigawa 2004; 2005], they are limited to simple geometries, certain types of gradation of material properties (for example, exponential or power law distribution), special types of boundary conditions and loadings. The above constraints can be relaxed when numerical approaches are applied. In those with finite element methods [Takahashi et al. 1992; Reddy and Chin 1998; Praveen et al. 1999; Wang and Mai 2005], homogeneous elements with different effective material properties are often used to model the macro, nonhomogeneous nature of FGCs. To better treat the nonhomogeneity of the material properties, meshless methods may

Keywords: functionally graded composites, thermomechanics, temperature-dependent material properties, micromechanical model, meshless local Petrov–Galerkin method.

provide a more cost-effective approach for computer-aided design tools for FGM materials. One of the unique features of meshless methods is that only a set of scattered nodes that need not be connected to form closed polygons is required to model the physical domain. They not only can avoid the numerical difficulties of mesh entanglement and distortion during high intensity loading interactions as often encountered in finite element and finite difference analyses, but lend themselves a natural way to treat initiation and growth of voids/cracks as well. It is not our intention to give an exhaustive review for the meshless particle methods; interested readers should refer to the literature for details. One of the well-known meshless methods is the meshless local Petrov–Galerkin (MLPG) method proposed by Atluri and Zhu [1998]. It is a truly mesh-free approach in terms of both interpolation of variables and integration of energy because it does not require a background mesh to evaluate various integrals appearing in the local weak formulation of the problem. Recently, the MLPG method has successfully been employed in the thermomechanical analysis of FGCs [Qian and Ching 2004; Qian and Batra 2004; 2005; Sladek et al. 2003; 2005; Ching and Yen 2005; Ching and Chen 2006].

Most of the theoretical investigations reported so far have not taken into account the temperature dependence for the material properties. Therefore, those results in general are only adequate for small change of temperature in an FGC or the variation of material properties against temperature being insignificant. To accurately describe thermomechanical behaviors of FGCs, temperature dependence on the material properties should be considered. To our knowledge, only a few studies have included the effects of temperature-dependent material properties [Praveen et al. 1999; Wang and Mai 2005; Wang and Tian 2005]. The first two works examine deformation and stress in a 1-D axisymmetric hollow cylinder, and the third solves transient heat conduction problems for a 1-D strip. All the effective temperature-dependent properties used are evaluated using the simple rule of mixture, which does not account for the interaction between phases, and thus only give rough approximate values for most of the effective properties. As pointed out by Ching and Chen [2006], the effective material properties evaluated by different homogenization schemes could lead to significantly different thermomechanical response for an FGC material. Accordingly, a higher fidelity, micromechanics based model should be employed in evaluation of the effective material properties.

In this paper, thermomechanical response of a linearly elastic FGC under temperature loading is investigated by using the MLPG method. The FGCs considered consist of spherical particulates ZrO_2 and alloy matrix Ti-6Al-4V with the volume fraction varying over a predefined direction. For simplicity, it is modeled as a macro nonhomogeneous, isotropic, 2-D body. To accurately predict their thermomechanical response, both the temperature-dependent thermophysical and thermomechanical properties of the constituents are employed. The effective material properties of the FGC are evaluated with the micromechanical models. A hollow FGC cylinder is first studied with the effective material properties estimated by the rule of mixtures to validate the present MLPG solution with the finite element result [Wang and Mai 2005]. Then, parametric studies are performed with respect to different profiles of graded FGCs, for a clamped-clamped thick beam and a square plate with a central hole. The impact of temperature dependence for the material properties on thermo-mechanical response prediction of FGCs in elevated temperature environments is investigated.

2. Governing equations

Consider a 2-D isotropic solid occupying the domain Ω bounded by the boundary Γ and unstressed at a reference temperature. In rectangular Cartesian coordinates $\boldsymbol{x} = [x_1\ x_2]^T$, (where the superscript T denotes transposition), the governing equations of elastostatics neglecting body forces and steady-state thermal equilibrium in the absence of internal heat sources are given by

$$\sigma_{ij,j} = 0 \quad \text{in } \Omega, \tag{1}$$

$$q_{j,j} = 0 \quad \text{in } \Omega, \tag{2}$$

where σ_{ij} and q_j are the components of the Cauchy stress tensor and the heat flux vector, respectively. A comma followed by index j denotes the partial differentiation with respect to coordinate x_j of a material point, and a repeated index implies summation over the range of the index. Equations (1) and (2) are supplemented with the boundary conditions

$$u_i = \bar{u}_i \ \text{ on } \Gamma_u, \qquad \sigma_{ij} n_j = \bar{t}_i \ \text{ on } \Gamma_t \tag{3}$$

and

$$T = \bar{T} \ \text{ on } \Gamma_T, \qquad q_j n_j = \bar{q} \ \text{ on } \Gamma_q, \qquad q_j n_j = h(T - T_s) \ \text{ on } \Gamma_h. \tag{4}$$

In these equations the u_i are the displacement components, T is the change of temperature with respect to a reference state, $\bar{u}_i$ are the prescribed displacements on Γ_u and $\bar{t}_i$ are the given tractions on Γ_t where Γ_u and Γ_t are the complementary parts of the boundary Γ, that is, $\Gamma_u \cap \Gamma_t = \varnothing$ and $\Gamma_u \cup \Gamma_t = \Gamma$. The thermal conditions include a prescribed temperature $\bar{T}$ specified on Γ_T, a given heat flux $\bar{q}$ imposed on Γ_q, and a convection heat loss to an ambient temperature T_s occurring on Γ_h. Likewise, Γ_T, Γ_q and Γ_h constitute another set of complementary parts of the boundary. h is the coefficient of the convection, and n_j are the components of the unit outward normal to Γ.

The constitutive equation for thermal stresses is written in the matrix form

$$\boldsymbol{\sigma} = \begin{bmatrix} \sigma_{11} & \sigma_{22} & \sigma_{12} \end{bmatrix}^T = \boldsymbol{D}\boldsymbol{\varepsilon} - \boldsymbol{\beta} T,$$

$\boldsymbol{\varepsilon}$ is the infinitesimal strain vector

$$\boldsymbol{\varepsilon} = \begin{bmatrix} \varepsilon_{11} & \varepsilon_{22} & \gamma_{12} \end{bmatrix}^T = \begin{bmatrix} \dfrac{\partial u_1}{\partial x_1} & \dfrac{\partial u_2}{\partial x_2} & \dfrac{\partial u_2}{\partial x_1} + \dfrac{\partial u_1}{\partial x_2} \end{bmatrix}^T, \tag{5}$$

$\boldsymbol{D}$ is the stiffness matrix and β is the stress-temperature matrix. For a linearly elastic, isotropic 2-D solid

$$\boldsymbol{D} = \frac{\bar{E}}{1-\bar{v}^2} \begin{bmatrix} 1 & \bar{v} & 0 \\ \bar{v} & 1 & 0 \\ 0 & 0 & \frac{1}{2}(1-\bar{v}) \end{bmatrix}, \qquad \boldsymbol{\beta} = \beta \begin{bmatrix} 1 & 1 & 0 \end{bmatrix}^T$$

in which $\bar{E} = E/(1-v^2)$, $\bar{v} = v/(1-v)$, and $\boldsymbol{\beta} = \alpha E/(1-2v)$ for plane strain with E, v and α denoting the Young's modulus, Poisson's ratio, and coefficient of thermal expansion, respectively, and $\bar{E} = E$, $\bar{v} = v$, and $\beta = \alpha E/(1-v)$ for plane stress. The Fourier law for heat flux is $q_j = -\kappa T_{,j}$, where κ is the thermal conductivity. For an FGC material, the material properties E, v, α, κ are functions of $\boldsymbol{x}$ in general.

3. The MLPG formulation

3.1. ***Nodal interpolation.*** In the MLPG method [Atluri and Zhu 1998] the moving least squares approximation is adopted for forming the basis functions $\phi_i(\boldsymbol{x})$ for an unknown trial function. Let $f^h(\boldsymbol{x})$ be an approximation of a scalar function $f(\boldsymbol{x})$ given by

$$f^h(\boldsymbol{x}) = \boldsymbol{p}^T(\boldsymbol{x})\boldsymbol{a}(\boldsymbol{x}) = \sum_{j=1}^{m} p_j(\boldsymbol{x})a_j(\boldsymbol{x}), \tag{6}$$

where $\boldsymbol{p}(x_1, x_2) = [p_1(\boldsymbol{x})\ p_2(\boldsymbol{x})\ \ldots\ p_m(\boldsymbol{x})]^T$ is a vector of the complete monomial basis of order m. For a 2-D problem, $\boldsymbol{p}(x_1, x_2) = [1\ x_1\ x_2]^T$ for $m = 3$ and $\boldsymbol{p}(x_1, x_2) = [1\ x_1\ x_2\ x_1^2\ x_1x_2\ x_2^2]^T$ for $m = 6$. The m unknown coefficients $a_j(\boldsymbol{x})$ are determined by minimizing a weighted discrete L_2 norm given as

$$J = \sum_{i=1}^{n} W(\boldsymbol{x} - \boldsymbol{x}_i)\big[\boldsymbol{p}^T(\boldsymbol{x}_i)\boldsymbol{a}(\boldsymbol{x}) - \hat{f}_i\big]^2, \tag{7}$$

where n is the number of points in the neighborhood of point $\boldsymbol{x}$ for which the weight function $W(\boldsymbol{x}-\boldsymbol{x}_i) > 0$, and $\hat{f}_i$ refers to the nodal parameter of the function f.

Finding the extremum of J in Equation (7) with respect to $\boldsymbol{a}(\boldsymbol{x})$ leads to the system of linear equations

$$\boldsymbol{A}(\boldsymbol{x})\boldsymbol{a}(\boldsymbol{x}) = \boldsymbol{B}(\boldsymbol{x})\hat{\boldsymbol{f}}, \tag{8}$$

where the matrices $\boldsymbol{A}(\boldsymbol{x})$ and $\boldsymbol{B}(\boldsymbol{x})$ and the vector $\hat{\boldsymbol{f}}$ are

$$\begin{aligned}
\boldsymbol{A}(\boldsymbol{x}) &= \sum_{i=1}^{n} W(\boldsymbol{x} - \boldsymbol{x}_i)\boldsymbol{p}(\boldsymbol{x}_i)\boldsymbol{p}^T(\boldsymbol{x}_i),\\
\boldsymbol{B}(\boldsymbol{x}) &= \big[W(\boldsymbol{x} - \boldsymbol{x}_1)\boldsymbol{p}(\boldsymbol{x}_1)\ \ W(\boldsymbol{x} - \boldsymbol{x}_2)\boldsymbol{p}(\boldsymbol{x}_2)\ \ \ldots\ \ W(\boldsymbol{x} - \boldsymbol{x}_n)\boldsymbol{p}(\boldsymbol{x}_n)\big],\\
\hat{\boldsymbol{f}} &= \big[\hat{f}_1\ \ \hat{f}_2\ \ \ldots\ \ \hat{f}_n\big]^T.
\end{aligned}$$

Solving $\boldsymbol{a}(\boldsymbol{x})$ in Equation (8) and substituting it into Equation (6) results in the following relation for the nodal interpolation

$$f^h(\boldsymbol{x}) = \sum_{i=1}^{n} \phi_i(\boldsymbol{x})\hat{f}_i \qquad \text{with} \quad \phi_i(\boldsymbol{x}) = \sum_{j=1}^{m} p_j(\boldsymbol{x})[\boldsymbol{A}^{-1}(\boldsymbol{x})\boldsymbol{B}(\boldsymbol{x})]_{ji},$$

where $\phi_i(\boldsymbol{x})$ is called the basis function of the moving least squares approximation corresponding to node i. Note that $\phi_i(\boldsymbol{x}_j)$ need not equal the Kronecker delta δ_{ij}, and thus $\hat{f}_i \neq f^h(\boldsymbol{x}_i)$ in general. For the matrix $\boldsymbol{A}$ to be invertible the number of n points must not be smaller than m, that is, $n \geq m$. For $m = 3$ or 6, Chati and Mukherjee [2000] utilized the moving least squares approximation in their boundary node method and suggested that $15 \leq n \leq 30$ gives acceptable results for 2-D elastostatic problems.

In this study, the following Gaussian function is adopted as the weight function:

$$W(\boldsymbol{x} - \boldsymbol{x}_i) = \frac{\exp\big(-(d_i/c_i)^{2k}\big) - \exp\big(-(r_i/c_i)^{2k}\big)}{1 - \exp\big(-(r_i/c_i)^{2k}\big)} \qquad \text{for} \quad 0 \leq d_i \leq r_i,$$

where c_i is the distance from node i to its third nearest neighboring node, d_i is the distance $|\boldsymbol{x} - \boldsymbol{x}_i|$, and r_i is the radius of the circle outside of which $W(\boldsymbol{x} - \boldsymbol{x}_i)$ vanishes, that is, $W = 0$ when $d_i > r_i$. We choose $m = 6$, $k = 1$ and $r_i = 4c_i$.

3.2. ***Weak formulation and discretization.*** This section presents weak (or variational) formulations corresponding to the governing equations (1)–(2) and the boundary conditions (3)–(4). The system equations are obtained by discretizing the weak formulation using the moving least squares method.

Thermoelastic analysis. Let $\boldsymbol{\xi}(\boldsymbol{x}) = [\xi_1\ \xi_2]^T$ be a set of two linearly independent test functions defined in Ω. We can obtain a useful relation by taking the inner product of Equation (1) with $\boldsymbol{\xi}$ and of Equation (3), left, with $\chi\boldsymbol{\xi}$, integrating the resulting equations over Ω and Γ_u, respectively, and adding them. To simplify it we integrate by parts, use the divergence theorem and impose the natural boundary condition from Equation (3), right, on Γ_t, obtaining

$$\int_\Omega \tilde{\boldsymbol{\varepsilon}}^T \boldsymbol{\sigma}\, d\Omega - \int_{\Gamma_u} \boldsymbol{\varepsilon}^T \boldsymbol{N}\boldsymbol{\sigma}\, d\Gamma - \int_{\Gamma_t} \boldsymbol{\varepsilon}^T \bar{\boldsymbol{t}}\, d\Gamma + \chi \int_{\Gamma_u} \boldsymbol{\varepsilon}^T (\boldsymbol{u} - \bar{\boldsymbol{u}})\, d\Gamma = 0, \tag{9}$$

where the strain vector $\tilde{\boldsymbol{\varepsilon}}$ is obtained from Equation (5) by replacing the displacement components u_i with the test functions ξ_i and matrix $\boldsymbol{N}$ is given by

$$\boldsymbol{N} = \begin{bmatrix} n_1 & 0 & n_2 \\ 0 & n_2 & n_1 \end{bmatrix}.$$

In Equation (9) χ is a penalty parameter. The penalty method is chosen here for imposing the essential boundary condition in the equations $u_i = \bar{u}_i$ and $T = \bar{T}$ from (3) and (4), due to the lack of the Kronecker delta property of the basis functions. Selection of the value of the penalty parameter still remains a challenge as the parameter cannot be taken "very large" in order to avoid the case of the system matrix being ill-defined. A suitable range for the value of the penalty parameter suggested by Zhu and Atluri [1998] is $\chi = (10^3 \sim 10^7) \cdot E$.

The most distinguished feature of the MLPG method is that the weak formulation is based on a local subdomain rather than a global problem domain. Consider that N nodes are in the domain Ω and $S_1, S_2, \ldots, S_N$ are smooth 2-D closed regions, not necessarily disjointed or having the same shape and size. Let $\{\phi_1, \phi_2, \ldots, \phi_n\}$ and $\{\psi_1, \psi_2, \ldots, \psi_n\}$ be two sets of linearly independent functions defined over a region, say S_α. The unknown trial function $\boldsymbol{u}$ and the test function $\boldsymbol{\xi}$ can respectively be expressed as

$$\boldsymbol{u}(\boldsymbol{x}) = \begin{bmatrix} u_1(\boldsymbol{x}) \\ u_2(\boldsymbol{x}) \end{bmatrix} = \sum_{J=1}^{n} \boldsymbol{\Phi}_J(\boldsymbol{x}) \widehat{\mathbf{u}}_J, \qquad \boldsymbol{\xi}(\boldsymbol{x}) = \begin{bmatrix} \xi_1(\boldsymbol{x}) \\ \xi_2(\boldsymbol{x}) \end{bmatrix} = \sum_{I=1}^{n} \boldsymbol{\Psi}_I(\boldsymbol{x}) \widehat{\xi}_I, \tag{10}$$

where $\boldsymbol{\Phi}_J = \phi_J \boldsymbol{I}$, $\boldsymbol{\Psi}_I = \psi_I \boldsymbol{I}$ with $\boldsymbol{I}$ a 2×2 identity matrix and $\widehat{\mathbf{u}}_J, \widehat{\xi}_I$ are 2×1 arrays. Various options of the test function that lead to different MLPG formulations have been discussed by Atluri [2005]. Here we equal the test function to the weight function of the moving least squares approximation. Thus, the strain vectors $\boldsymbol{\varepsilon}$ and $\tilde{\boldsymbol{\varepsilon}}$ become

$$\boldsymbol{\varepsilon} = \sum_{J=1}^{n} \boldsymbol{B}_J \widehat{\mathbf{u}}_J, \qquad \tilde{\boldsymbol{\varepsilon}} = \sum_{I=1}^{n} \tilde{\boldsymbol{B}}_I \widehat{\xi}_I, \tag{11}$$

where

$$\boldsymbol{B}_J = \begin{bmatrix} \frac{\partial \phi_J}{\partial x_1} & 0 \\ 0 & \frac{\partial \phi_J}{\partial x_2} \\ \frac{\partial \phi_J}{\partial x_2} & \frac{\partial \phi_J}{\partial x_1} \end{bmatrix}, \qquad \tilde{\boldsymbol{B}}_I = \begin{bmatrix} \frac{\partial \psi_I}{\partial x_1} & 0 \\ 0 & \frac{\partial \psi_I}{\partial x_2} \\ \frac{\partial \psi_I}{\partial x_2} & \frac{\partial \psi_I}{\partial x_1} \end{bmatrix}.$$

Replacing the domain Ω of integration in Equation (9) by S_α, substituting for $\boldsymbol{u}$, $\boldsymbol{\xi}$, $\boldsymbol{\varepsilon}$, and $\tilde{\boldsymbol{\varepsilon}}$ from Equations (10) and (11), and requiring that the resulting equations hold for all choices of $\widehat{\xi}_I$, one arrives at the following linear algebraic equations for $\widehat{\mathbf{u}}_J$:

$$\sum_{J=1}^{n} \int_{S_\alpha} \tilde{\boldsymbol{B}}_I^T \boldsymbol{D} \boldsymbol{B}_J \widehat{\mathbf{u}}_J \, d\Omega - \sum_{J=1}^{n} \int_{\Gamma_{\alpha u}} \boldsymbol{\Psi}_I^T \boldsymbol{S} \boldsymbol{N} \boldsymbol{D} \boldsymbol{B}_J \widehat{\mathbf{u}}_J \, d\Gamma + \sum_{J=1}^{n} \chi \int_{\Gamma_{\alpha u}} \boldsymbol{\Psi}_I^T \boldsymbol{S} \boldsymbol{\Phi}_J \widehat{\mathbf{u}}_J \, d\Gamma$$
$$= \int_{S_\alpha} \tilde{\boldsymbol{B}}_I^T \boldsymbol{\beta} T \, d\Omega - \int_{\Gamma_{\alpha u}} \boldsymbol{\Psi}_I^T \boldsymbol{S} \boldsymbol{N} \boldsymbol{\beta} T \, d\Omega + \int_{\Gamma_{\alpha t}} \boldsymbol{\Psi}_I^T \bar{\boldsymbol{t}} \, d\Gamma + \chi \int_{\Gamma_{\alpha u}} \boldsymbol{\Psi}_I^T \bar{\boldsymbol{u}} \, d\Gamma \quad (12)$$

for $I = 1, 2, \ldots, n$, where

$$\boldsymbol{S} = \begin{bmatrix} S_1 & 0 \\ 0 & S_2 \end{bmatrix}, \qquad S_i = \begin{cases} 1 & \text{if } u_i \text{ is prescribed on } \Gamma_{\alpha u}, \\ 0 & \text{if } u_i \text{ is not prescribed on } \Gamma_{\alpha u}. \end{cases}$$

Symbolically, the simultaneous Equation (12) are written in the matrix form

$$\boldsymbol{K}_\alpha \widehat{\mathbf{u}}_\alpha = \boldsymbol{F}_\alpha. \quad (13)$$

The final system of equations can be obtained by assembling Equation (13) for all the N nodes over the entire domain.

Nonlinear heat conduction analysis. Let $\eta(\boldsymbol{x})$ be another test function defined over Ω. Following the procedure in the above thermoelastic analysis yields the weak form associated with the governing Equation (2) and the boundary conditions given in Equation (4), we get

$$\int_\Omega (\nabla^T \eta) \boldsymbol{q} \, d\Omega - \int_{\Gamma_T} \eta \boldsymbol{n}^T \boldsymbol{q} \, d\Gamma - \int_{\Gamma_q} \eta \bar{\boldsymbol{q}} \, d\Gamma - \int_{\Gamma_h} \eta h (T - T_s) \, d\Gamma + \chi \int_{\Gamma_T} \eta (T - \bar{T}) \, d\Gamma = 0, \quad (14)$$

where $\boldsymbol{q} = [q_1 \;\; q_2]^T$ and $\boldsymbol{n} = [n_1 \;\; n_2]^T$. With the unknown trial function T and the test function η expressed in an interpolative form as

$$T(\boldsymbol{x}) = \sum_{J=1}^{n} \phi_J(\boldsymbol{x}) \widehat{T}_J, \qquad \eta(\boldsymbol{x}) = \sum_{I=1}^{n} \psi_I(\boldsymbol{x}) \widehat{\eta}_I \quad (15)$$

one has

$$\nabla T = \sum_{J=1}^{n} \boldsymbol{C}_J \widehat{T}_J, \qquad \nabla \eta = \sum_{I=1}^{n} \tilde{\boldsymbol{C}}_I \widehat{\eta}_I, \quad (16)$$

where

$$\boldsymbol{C}_J = \begin{bmatrix} \frac{\partial \phi_J}{\partial x_1} \\ \frac{\partial \phi_J}{\partial x_2} \end{bmatrix}, \qquad \tilde{\boldsymbol{C}}_J = \begin{bmatrix} \frac{\partial \psi_J}{\partial x_1} \\ \frac{\partial \psi_J}{\partial x_2} \end{bmatrix}.$$

Substituting for $T, \eta, \nabla T, \nabla\eta$ from Equations (15) and (16) into Equation (14) for a region S_α and requiring that the resulting equations hold for every choices of $\widehat{\eta}_I$, we arrive at the following simultaneous equations for $I = 1, 2, \ldots, n$

$$\sum_{J=1}^{n} \boldsymbol{L}_{IJ}(T)\widehat{T}_J = \sum_{J=1}^{n} \boldsymbol{G}_I, \tag{17}$$

where

$$\boldsymbol{L}_{IJ} = \int_{S_\alpha} \tilde{\boldsymbol{C}}_I^T \kappa \boldsymbol{C}_J \, d\Omega - \int_{\Gamma_{\alpha T}} \boldsymbol{\psi}_I \kappa \boldsymbol{n}^T \boldsymbol{C}_J \, d\Gamma + \int_{\Gamma_{\alpha h}} h\boldsymbol{\psi}_I \boldsymbol{\phi}_J \, d\Gamma - \chi \int_{\Gamma_{\alpha T}} \boldsymbol{\psi}_I \boldsymbol{\phi}_J \, d\Gamma, \tag{18}$$

$$\boldsymbol{G}_I = -\int_{\Gamma_{\alpha q}} \boldsymbol{\psi}_I \bar{q} \, d\Gamma - \chi \int_{\Gamma_{\alpha T}} \boldsymbol{\psi}_I \bar{T} \, d\Gamma + \int_{\Gamma_{\alpha h}} h\boldsymbol{\psi}_I \bar{T}_s \, d\Gamma. \tag{19}$$

Repeating Equation (17) for all the N nodes in the domain leads to the system of equations for the temperature field. It should be noted that the first two terms on the right-hand side of Equation (18) become nonlinear if the thermal conductivity is temperature-dependent. Hence the system of equations needs to be solved iteratively. The Newton–Raphson method [Cook et al. 1989] is adopted to solve the system of equations here. The solution is assumed to have converged when the criterion

$$\sqrt{\sum_{i=1}^{N} (\widehat{T}_i^{j+1} - \widehat{T}_i^{j})^2} \Bigg/ \sqrt{\sum_{i=1}^{N} \widehat{T}_i^{j^2}} < 10^{-4}, \tag{20}$$

is met, where the superscript j denotes the iteration number.

To utilize the Gauss quadrature rule to evaluate the domain integral on S_α and the line integrals on ∂S_α in Equations (12), (18) and (19), the region S_α and its boundaries $\Gamma_{\alpha u}, \Gamma_{\alpha t}, \Gamma_{\alpha q}, \Gamma_{\alpha T}$ and $\Gamma_{\alpha h}$ are mapped onto a $[-1, 1] \times [-1, 1]$ square domain and a $[-1, 1]$ straight line, respectively. Using this approach no shadow cells are needed for the integration.

4. Temperature-dependent material properties and effective moduli

In this study a ceramic ZrO_2 is taken as the particulate phase and alloy Ti-6Al-4V as the matrix phase. For practice the FGC is treated as a macro-nonhomogeneous isotropic material. The temperature-dependent material properties of the two constituents are given as follows [Tanigawa et al. 1997]:

$$\begin{aligned} ZrO_2: \quad & E = 132.2 - 50.3 \times 10^{-3}T - 31.4 \times 10^{-6}T^2 \ \text{(GPa)}, \\ & \nu = 0.333, \\ & \kappa = 1.71 + 0.21 \times 10^{-3}T + 0.116 \times 10^{-6}T^2 \ (W/mK) \\ & \alpha = 13.31 \times 10^{-6} - 18.9 \times 10^{-9}T + 12.7 \times 10^{-12}T^2 \ (1/K), \end{aligned} \tag{21}$$

$$\begin{aligned} \text{Ti-6Al-4V:} \quad & E = 122.7 - 0.0565T \ \text{(GPa)}, \\ & \nu = 0.289 + 32.0 \times 0^{-6}T, \\ & \kappa = 1.1 + 0.017T \ (W/mK), \\ & \alpha = 7.43 \times 10^{-6} - 5.56 \times 10^{-9}T + 2.69 \times 10^{-12}T^2 \ (1/K). \end{aligned} \tag{22}$$

The Poisson's ratio ν of ZrO_2 is assumed to be constant here since its dependence on temperature may be weak [Dole and Hunter Jr. 1983]. The first (constant) terms in Equations (21) and (22) are the material properties at temperature $T = 0°K$, which is assumed as the reference state temperature in this work. At elevated temperatures, for example, $T = 1000°K$, the changes of the Young's modulus, thermal conductivity, and coefficient of thermal expansion are about -61.8%, 19.1%, and -46.6%, respectively, for ZrO_2 and about -46.1%, 1545.5% and -38.6% respectively for Ti-6Al-4V. Due to the nontrivial change of the material properties, a significant difference of the thermomechanical response prediction can be expected when the constant properties are used. To delineate the influence of temperature dependence for the material properties on thermomechanical response of the FGCs, both the temperature-dependent and constant material properties are incorporated in this paper.

Two homogenization schemes are frequently utilized to evaluate the effective material properties for composites. One is the rule of mixtures, and the other is the micromechanical model. The former is simple to use but does not include the effect of interaction between the different constituents. For a two-phase composite it computes the effective value of a composite material property (P) by

$$P = P_m V_m + P_c V_c, \tag{23}$$

where subscripts m and c are associated with the matrix and particulate phase, respectively; the volume fractions satisfy $V_m + V_c = 1$. On the other hand, the latter evaluates the effective properties of a composite based on elasticity theory by considering the inclusion of particulates or fibers in a matrix phase.

Several micromechanical models have been derived for the effective properties of composite materials [Christensen 1979]. For a two-phase particulate composite the effective bulk and shear moduli K, μ derived by Mori and Tanaka [1973] are given as

$$\frac{K - K_m}{K_c - K_m} = \frac{V_c}{1 + (1 - V_c)(K_c - K_m)/(K_m + 4\mu_m/3)}, \tag{24}$$

$$\frac{\mu - \mu_m}{\mu_c - \mu_m} = \frac{V_c}{1 + (1 - V_c)(\mu_c - \mu_m)/(\mu_m + f_m)}, \tag{25}$$

with $f_m = \mu_m(9K_m + 8\mu_m)/6(K_m + 2\mu_m)$. The effective Young's modulus and Poisson's ratio are related to the bulk and shear moduli by $E = 9K\mu/(3K + \mu)$ and $\nu = (3K - 2\mu)/2(3K + \mu)$, respectively. The effective thermal conductivity κ derived by Hatta and Taya [1985] and the coefficient of thermal expansion α derived by Rosen and Hashin [1970] are

$$\frac{\kappa - \kappa_m}{\kappa_c - \kappa_m} = \frac{V_c}{1 + (1 - V_c)(\kappa_c - \kappa_m)/3\kappa_m}, \qquad \frac{\alpha - \alpha_m}{\alpha_c - \alpha_m} = \frac{1/K - 1/K_m}{1/K_c - 1/K_m}. \tag{26}$$

5. Results and discussion

A computer code based on the aforementioned MLPG formulation was developed and used to analyze the steady-state thermoelastic response of 2-D FGCs in elevated temperature environments. Three examples are examined: (1) a hollow cylinder under a temperature change at internal surface, (2) a clamped-clamped thick beam with a temperature change on the top surface, and (3) a square plate with a central hole subjected to a temperature change either at the hole surface or the outer boundary. The effective properties of the FGCs are estimated with the rule of mixtures of Equation (23) for the first example for

comparison with the finite element solution and with the micromechanical models of Equations (24)–(26) for the other two examples.

5.1. ***A hollow cylinder under temperature change at internal surface.*** Here we consider a functionally graded hollow cylinder with the inner radius of $r_i = 50\,\text{mm}$ and outer radius of $r_o = 150\,\text{mm}$. Temperature at the inner surface is suddenly increased to $T_i = 1000^\circ K$ and then kept constant, while the temperature on the outer surface is fixed at the reference temperature, that is, $T_o = 0$. The volume fraction of ceramic phase ZrO_2 is assumed to have the radial dependence by a power-law function as

$$V_c = V_c^o + (V_c^i - V_c^o)\left(\frac{r_o - r}{r_o - r_i}\right)^n, \tag{27}$$

where V_c^i and V_c^o are, respectively, the volume fractions of ZrO_2 on the inner and outer surfaces, and n is the power law index that dictates the volume fraction profile across the thickness of the cylinder. With the symmetry boundary conditions, a quadrant of the circular cross-section of the cylinder is analyzed as though it were essentially a 1-D axisymmetric problem. A total of 21×40 nodes are equally spaced along the radial and circumferential directions, respectively. Plane strain condition is assumed. All the results presented below are normalized by

$$[\bar{r}, \bar{T}, \bar{u}_r, \bar{\sigma}_\theta] = \left[\frac{r}{r_i}, \frac{T}{T_i}, \frac{10u_r}{(r_o - r_i)\alpha_{Ti}^0 T_i}, \frac{10\sigma_\theta}{E_{Ti}^0 \alpha_{Ti}^0 T_i}\right],$$

where σ_θ, E_{Ti}^0 and α_{Ti}^0 are the hoop stress, the (constant) Young's modulus and thermal expansion coefficient of Ti-6Al-4V at $T = 0$.

Figure 1 shows the through-the-thickness variation of the temperature and hoop stress respectively, for the case of $V_c^i = 1$, $V_c^o = 0$ and $n = 1$. Apparently, the present MLPG solution agrees very well with

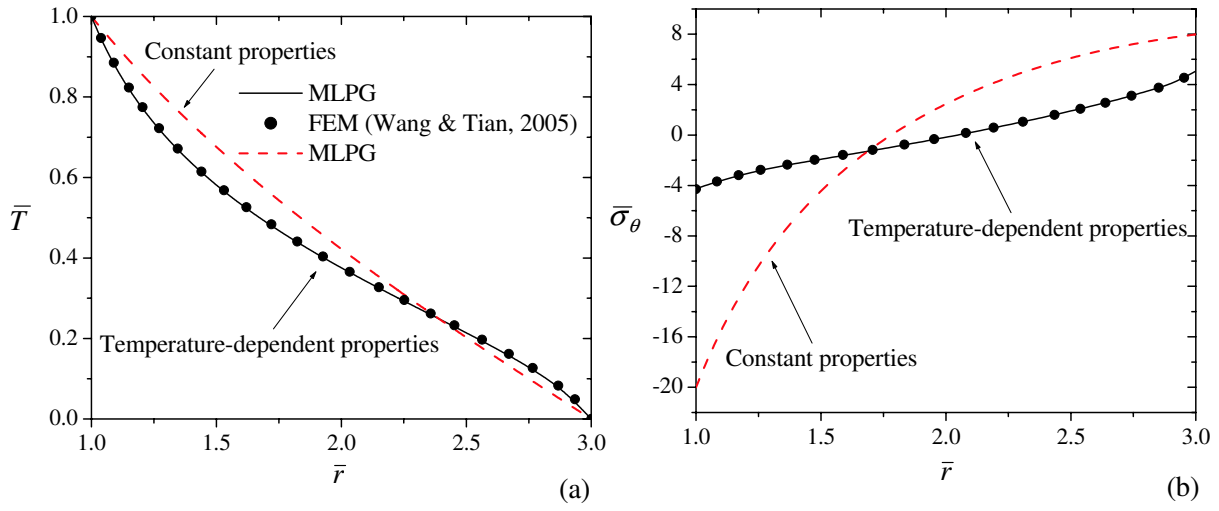

Figure 1. Through-the-thickness variations of the normalized (a) temperature change and (b) hoop stress obtained by the finite element method and MLPG method; effective material properties are computed by the rule of mixtures with $V_c^o = 0$, $V_c^i = 1$ and $n = 1$.

the 1-D axisymmetric finite element result [Wang and Mai 2005], which is obtained with 100 elements. The FGC in each element is assumed to be homogeneous but different from one another. In the present analysis 21 nodes are used through the thickness direction. The results computed with the constant material properties are also included in Figure 1. It can be seen from Figure 1(b) that the resulting hoop stress is quite different when the temperature dependence on the material properties is excluded. For example, the dimensionless hoop stress on the inner surface computed with the temperature-dependent material properties is about -4, and changes to -20 when the properties are assumed to be constant. The discrepancy found here suggests that the temperature dependence of material properties should not be ignored in thermomechanical analysis when an FGC is under severe thermal loading.

Figure 2 displays the through-the-thickness variation of the effective Young's modulus, Poisson's ratio, thermal conductivity, and coefficient of thermal expansion for the case of $V_c^i = 1$, $V_c^o = 0$ and $n = 1$,

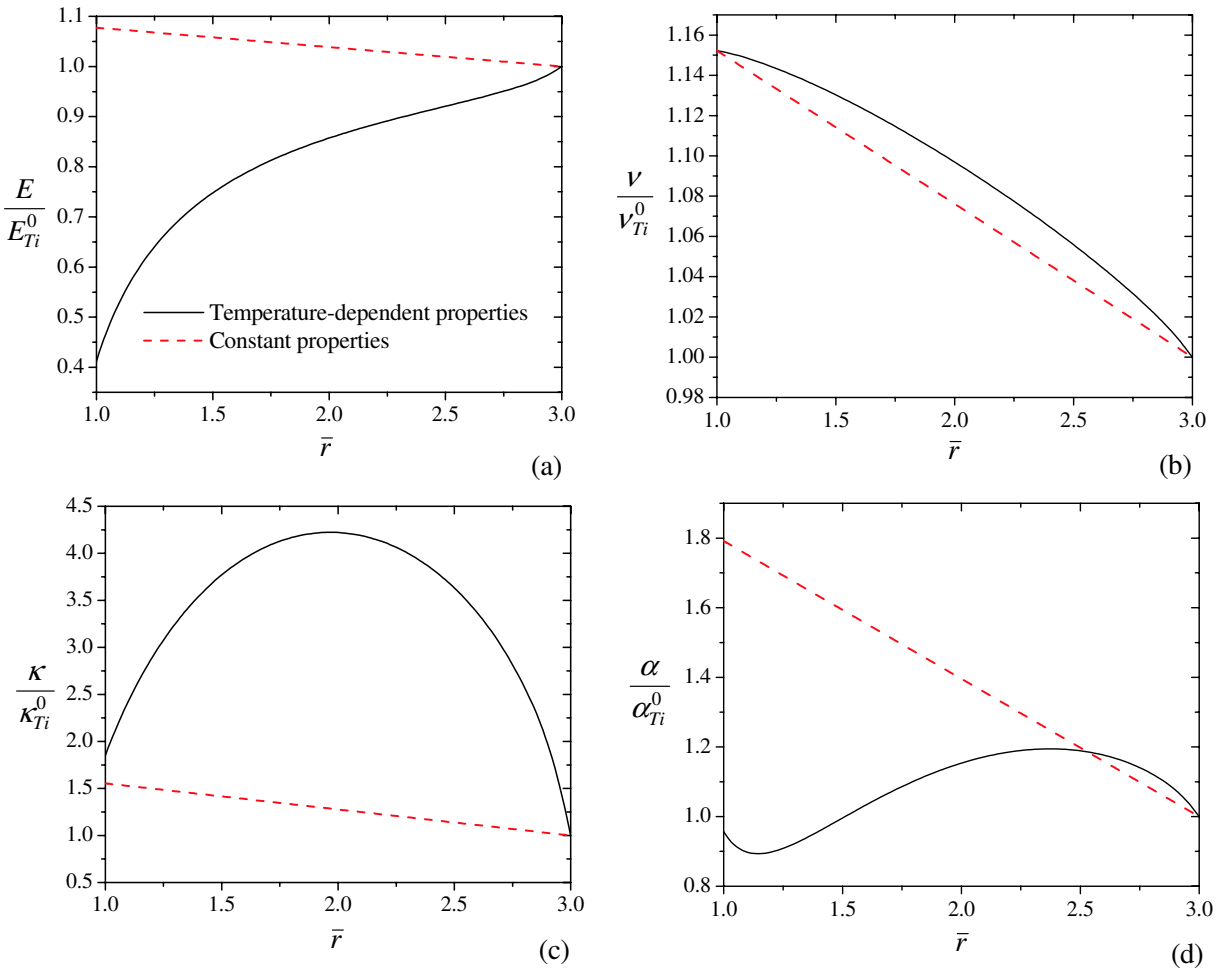

Figure 2. Through-the-thickness variations of effective material properties computed by the rule of mixtures for the case of $V_c^o = 0$, $V_c^i = 1$ and $n = 1$: (a) Young's modulus, (b) Poisson's ratio, (c) thermal conductivity; (d) coefficient of thermal expansion.

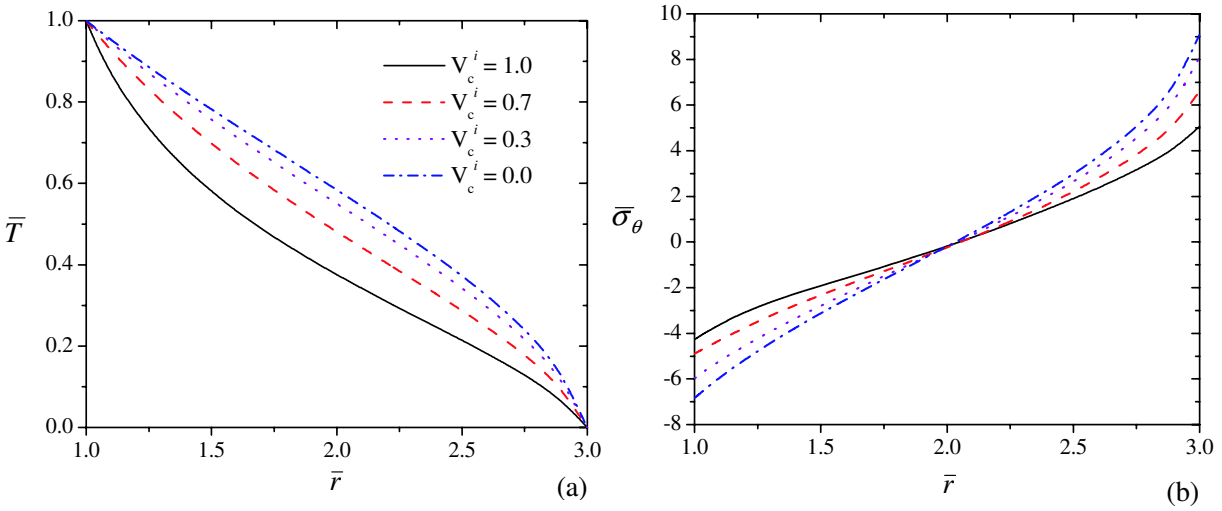

Figure 3. Distribution of the normalized (a) temperature change and (b) hoop stress over the thickness of the cylinder for different values of V_c^i with $V_c^o = 0$ and $n = 1$, calculated with the temperature-dependent material properties.

normalized by the corresponding constant properties of Ti-6Al-4V. For the case of constant material properties, all the properties are linear functions of r as dictated by Equation (27). However, the linear relations no longer exist when the temperature dependence of material properties is taken into account. Figure 2(a) shows that the effective Young's modulus monotonically increases from the inner surface to the outer surface, whereas the trend is opposite when the temperature dependence is neglected. The normalized values at the inner surface are 0.411 versus 1.08. Neither the thermal conductivity nor the coefficient of thermal expansion vary monotonically; see Figures 2(c) and 2(d).

Variations of the temperature change and hoop stress are further evidenced in Figure 3 for different values of V_c^i with $V_c^o = 0$ and $n = 1$, calculated with the temperature-dependent material properties. The case of $V_c^i = 0$ corresponds to a pure Ti-6Al-4V cylinder. Figure 3(a) shows the temperature decreases with increase of the ceramic content except for those at the inner and outer surface, where the temperatures remain constant specified by the boundary conditions. It is also found from Figure 3(b) that the magnitude of the hoop stress reduces as the ceramic ZrO_2 increases in the FGC.

Figure 4 shows the normalized radial displacement at the inner and outer surfaces as a function of n with $V_c^i = 1$ and $V_c^o = 0$. An increase of the value in n means that the FGC cylinder has more composition of Ti-6Al-4V. The pure ZrO_2 cylinder is the limit case of $n = 0$. By comparing the results in the two parts of the figure we can ascertain that the trend of net expansion of the wall thickness with n is opposite when the temperature dependence of the material properties is neglected. In addition, use of the constant material properties overestimates the net wall thickness expansion for small n, but underestimates the expansion for large n.

5.2. ***A clamped-clamped thick beam with temperature change on top surface.*** A clamped-clamped FGC beam of length $L = 50$ mm and thickness $H = 10$ mm is subjected to a sinusoidal temperature

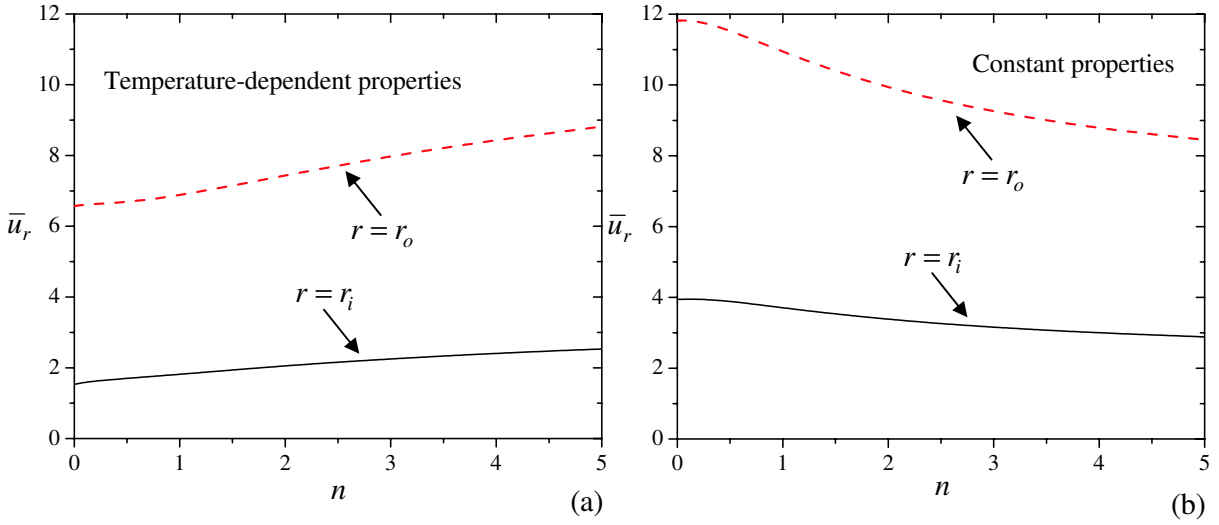

Figure 4. Variations of the normalized radial displacement on the inner and outer surfaces with the power law index n for $V_c^i = 1$ and $V_c^o = 0$: (a) temperature-dependent material properties and (b) constant material properties.

change $T = T_0 \sin(\pi x_1/L)$ with $T_0 = 1000°K$, on the top surface; see Figure 5. The bottom surface and the two edges of the beam are at the reference temperature. The origin of the rectangular Cartesian coordinates (x_1, x_2) is located at the left bottom corner of the beam, and the x_1-axis is parallel to the long edges. Plane strain condition is assumed. The volume fraction of the ceramics phase varies over the beam thickness by a power law function as

$$V_c = V_c^- + (V_c^+ - V_c^-)\left(\frac{x_2}{H}\right)^n, \tag{28}$$

where V_c^+ and V_c^- are the volume fractions of ZrO_2 on the top and the bottom surfaces, respectively, and n is the power law index. Instead of using the rule of mixtures, the effective material properties are computed with the micromechanical models described in Section 4.

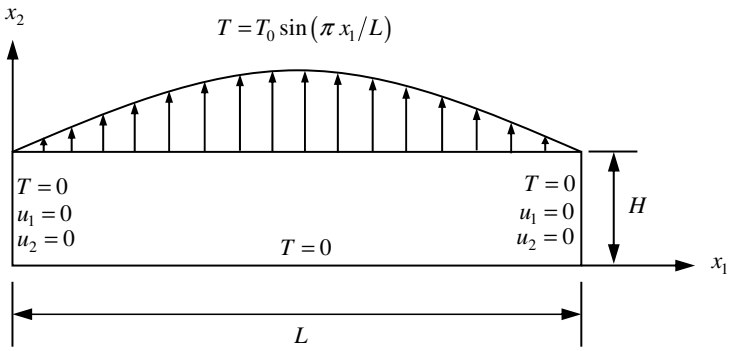

Figure 5. An FGC thick beam subjected to a sinusoidal temperature load on the top surface.

Due to the symmetry to the vertical centroidal plane, the left half of the domain is analyzed with a uniform mesh of 55 nodes along x_1-direction and 25 nodes along the x_2-direction, for which the solution has been tested to be convergent. The physical quantities presented below are normalized by

$$\left[\bar{x}_1, \bar{x}_2, \bar{T}, \bar{u}_2, \bar{\sigma}_{11}, \bar{\sigma}_{12}\right] = \left[\frac{x_1}{L}, \frac{x_2}{H}, \frac{T}{T_0}, \frac{10Hu_2}{\alpha_{Ti}^0 T_0 L^2}, \frac{10\sigma_{11}}{E_{Ti}^0 \alpha_{Ti}^0 T_0}, \frac{10L\sigma_{12}}{E_{Ti}^0 \alpha_{Ti}^0 T_0 H}\right]. \tag{29}$$

Figure 6 plots the distributions of the effective Young's modulus, thermal conductivity, and coefficient

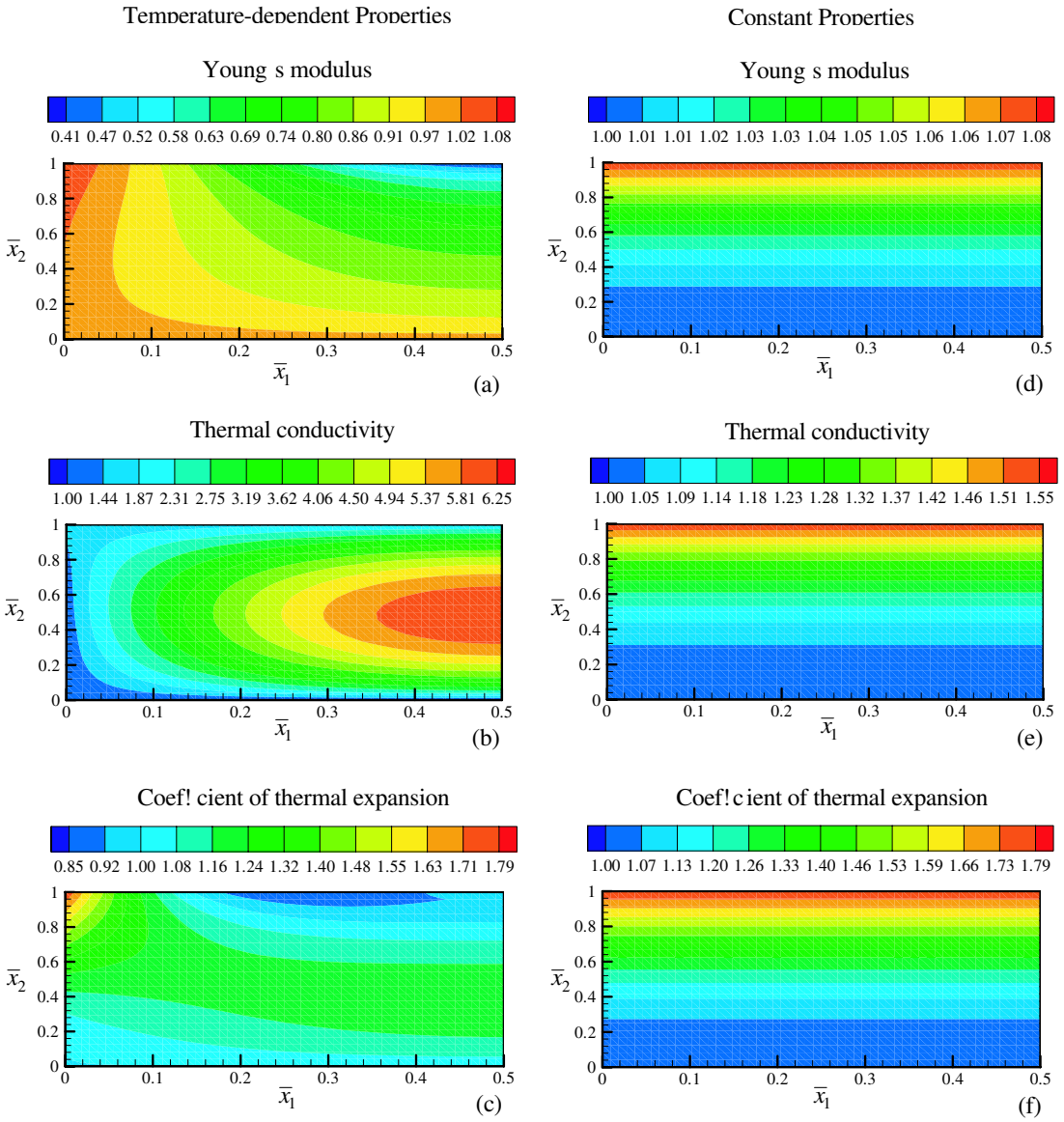

Figure 6. Distributions of normalized effective properties computed with $V_c^+ = 1$, $V_c^- = 0$ and $n = 2$.

of thermal expansion normalized by the corresponding constants of Ti-6Al-4V. The values of $V_c^+ = 1$, $V_c^- = 0$ and $n = 2$ were chosen. The left-hand panes of the figure clearly show that, for constant material properties, the dependence is on x_1 only and the maximum value always occurs on the top surface (pure ZrO_2), basically following the volume fraction distribution of ZrO_2 described by Equation (28). When the temperature dependence is included, the overall material properties no longer follow the graded material pattern; see left side of Figure 6.

Figure 7 shows the influence of temperature dependence of material properties on the deformation, temperature, and longitudinal stress (σ_{11}) in the beam for $V_c^+ = 1$, $V_c^- = 0$ and $n = 2$. The top row

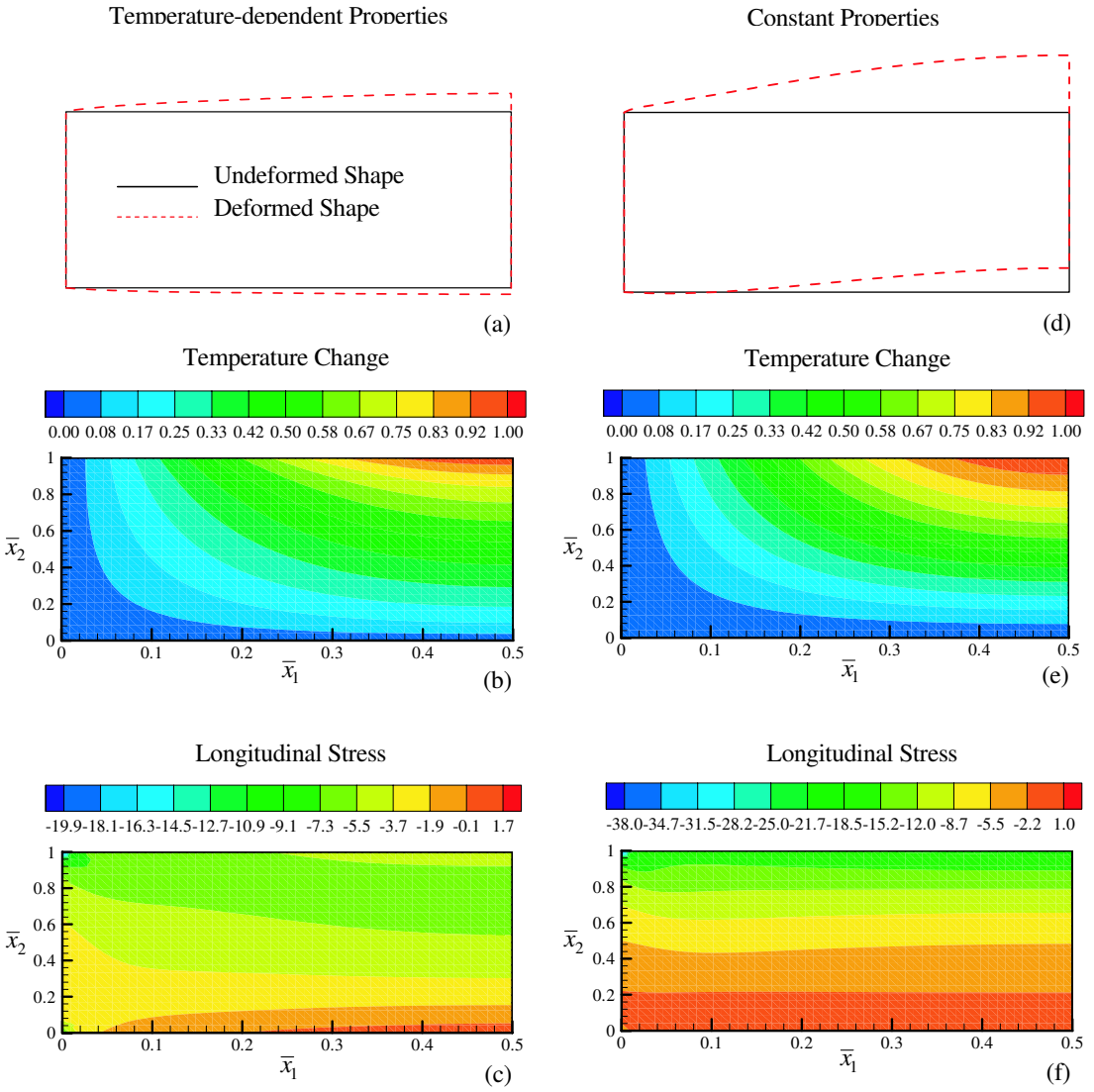

Figure 7. Comparison of the thermomechanical response of the FGC beam with $V_c^+ = 1$, $V_c^- = 0$ and $n = 2$ computed with temperature-dependent material properties and constant material properties; deformations in (a) and (d) are enlarged by 20 times.

shows that, when subjected to temperature rise on the top surface, the beam expands, but the amount of expansion is different between the two cases. Apparently, use of the constant material properties not only predicts a larger increase for the beam thickness, but a larger deflection as well. This can be seen by examining the values of $\alpha\Delta T$ and $\alpha E\Delta T$ over the thickness. The impact of the temperature dependence of material properties on the steady-state temperature response is less pronounced; see middle row of Figure 7. With the temperature dependence, the resulting maximum normalized longitudinal stress, however, can be decreased by nearly 100%, from -38.0 to -19.9; see bottom row of the figure.

Figure 8 displays the distribution of normalized temperature, transverse displacement, longitudinal stress, and transverse shear stress over the thickness of the FGC beam for four different values of V_c^+

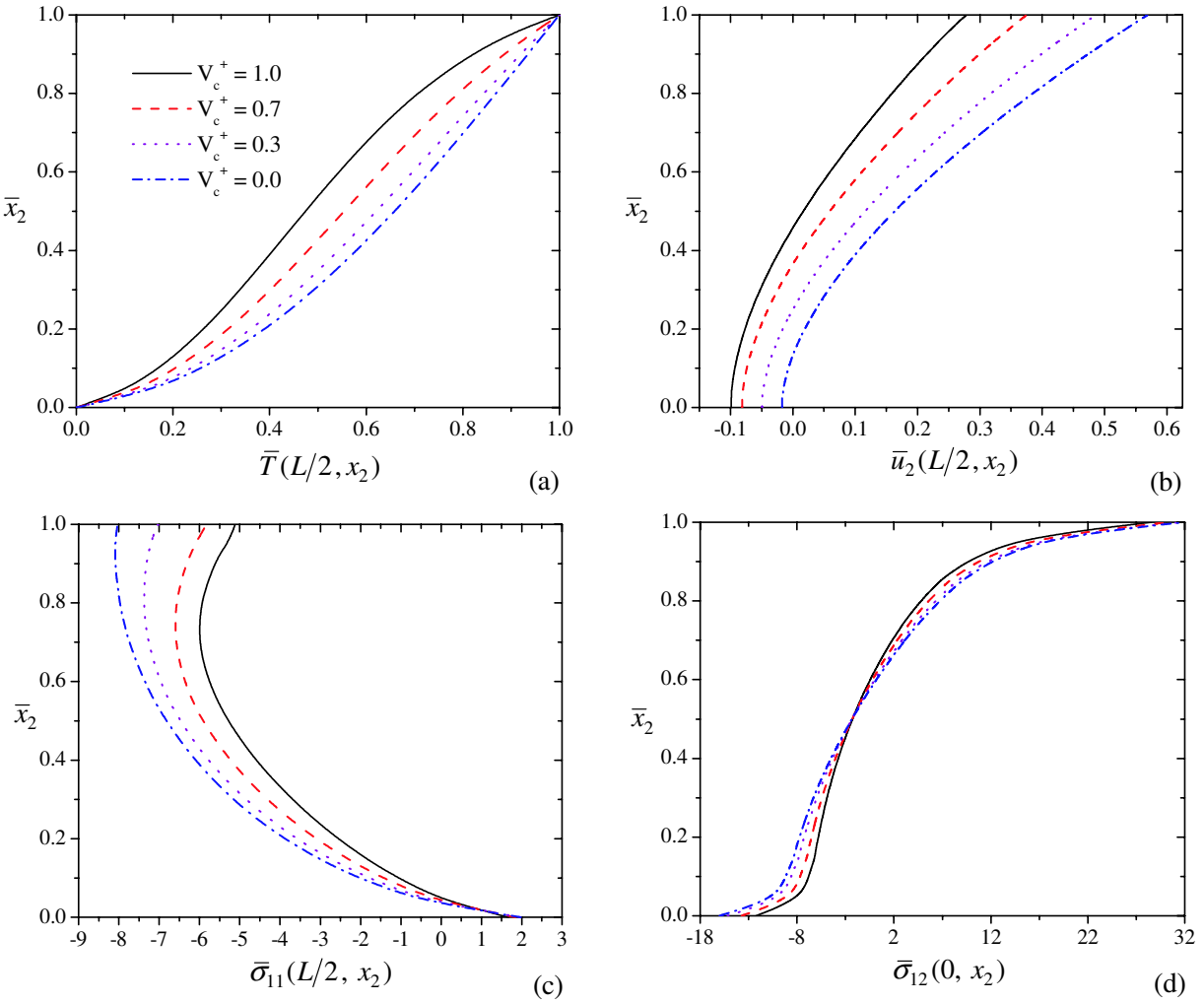

Figure 8. Distribution of the normalized (a) temperature change, (b) transverse displacement, (c) longitudinal stress, and (d) transverse shear stress over the thickness of the beam for different values of V_c^+ with $V_c^- = 0$ and $n = 2$, computed with the temperature-dependent material properties.

with $V_c^- = 0$ and $n = 2$. These results are calculated with the temperature-dependent material properties. Like the results in the previous cylinder case, the temperature change, transverse displacement and the magnitude of stresses all decrease as V_c^+ increases.

Figure 9 illustrates the temperature change, transverse displacement, longitudinal stress, and transverse shear stress as functions of the power index n at some points of interest. Again, the significant differences between the two cases found here reveal the importance of the temperature dependence of material properties in simulation of thermomechanical response of the FGCs in elevated temperature environments.

5.3. ***A square plate with a central hole under temperature change along boundaries.*** The analysis for a centrally-holed FGC square plate under the temperature change along boundaries is conducted. The

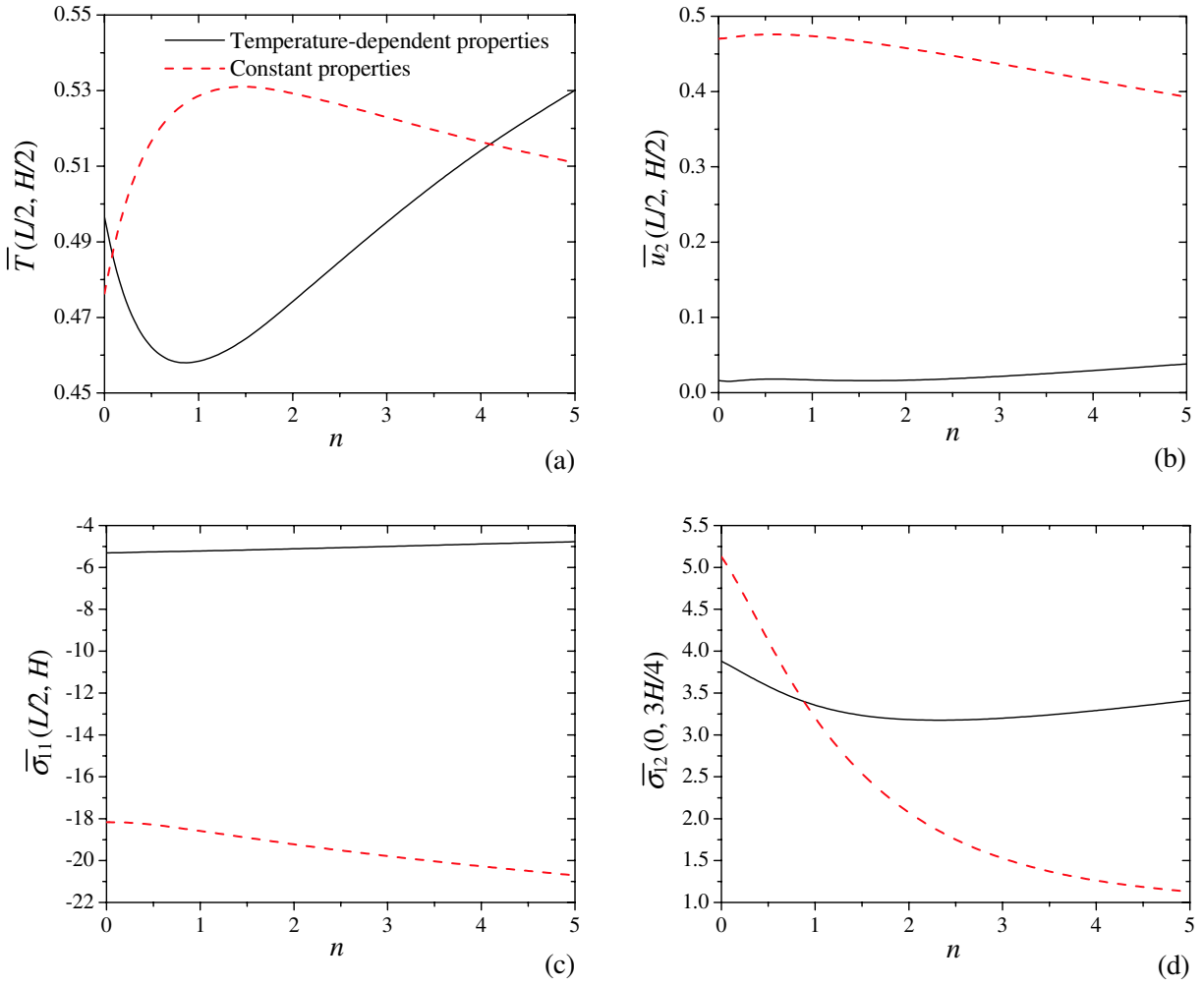

Figure 9. The normalized (a) temperature change, (b) transverse displacement, (c) longitudinal stress, and (d) transverse shear stress at some points of interest in the FGC beam as functions of the power law index n with $V_c^+ = 1$, $V_c^- = 0$.

edge length of the plate is $L = 4\,\text{mm}$ and the radius of the hole is $r_a = 1.5\,\text{mm}$. The origin of the rectangular Cartesian coordinates (x_1, x_2) coincides with the center of the hole, and the x_1-axis points to the middle point of the right vertical edge. For convenience, a polar coordinate system (r, θ) is also set at the center of the hole with θ measured counterclockwise from the positive x_1-axis. The volume fraction of the ceramic is assumed to vary along the radial direction r with

$$V_c = V_c^- + (V_c^+ - V_c^-)\left(\frac{r - r_a}{r_d - r_a}\right)^n,$$

where r_d is the radial distance measured from a point on the surface of the hole to the corresponding point at the outer boundary of the plate and V_c^+ and V_c^- are the volume fractions of ZrO_2 at the outer boundary and the hole surface, respectively. Two temperature loadings are considered: (a) a temperature rise of $T_0 = 1000°K$ is applied on the outer boundary while the surface of the hole is kept at $T = 0$, and (b) a temperature rise of $T_0 = 1000°K$ is applied on the surface of the hole while the outer boundary is kept at $T = 0$. Since a ceramic-rich layer usually is in the hotter region, $V_c^+ = 1.0$ and $V_c^- = 0$ are assumed for the loading condition (a) and $V_c^+ = 0$ and $V_c^- = 1.0$ for the condition (b). Plane stress condition is assumed.

Only the first quadrant of the plate is analyzed with the symmetric boundary conditions imposed on the x_1- and x_2-axis. A total of 1025 nodes, the effect of which passed the convergence test for the nodal density, is meshed. The results presented below are normalized as follows

$$\left[\bar{x}_1, \bar{x}_2, \bar{\sigma}_{22}, \bar{\sigma}_\theta, \bar{\sigma}_e\right] = \left[\frac{x_1}{a}, \frac{x_2}{a}, \frac{10\sigma_{22}}{E_{Ti}^0 \alpha_{Ti}^0 T_0}, \frac{10\sigma_\theta}{E_{Ti}^0 \alpha_{Ti}^0 T_0}, \frac{10\sigma_e}{E_{Ti}^0 \alpha_{Ti}^0 T_0}\right].$$

The normal stress $\bar{\sigma}_{22}$ along the x_1-axis and the hoop stress $\bar{\sigma}_\theta$ around the surface of the hole for different values of n are presented in Figure 10 for condition (a). As expected, the stress σ_{22} is in tension near the hole and in compression near the edge regardless of the value of n. It is clear from the top row of Figure 10 that for the case of temperature-dependent material properties the magnitude of σ_{22} increases as n increases; however, the trend is opposite when temperature dependence is excluded. The tensile stress σ_{22} in the region near the hole computed with the temperature-dependent material properties increases as n decreases. A similar conclusion also applies to the hoop stress σ_θ around the surface of the hole; see bottom row of the figure. Maximum σ_θ occurs at $\theta = 0, \pm\pi/2$ and π, while the minimum occurs at $\theta = \pm\pi/4$ and $\pm 3\pi/4$.

Figure 11 compares the normalized effective stress $\bar{\sigma}_e$ in the plate for $n = 2$, calculated with and without the temperature dependence on the material properties. It appears that the peak effective stress occurs at the intersections between the surface of the hole and the x_1- and x_2-axis. A comparison of the values of $\bar{\sigma}_e$ in the two halves of Figure 11 indicates that use of the constant material properties would underpredict the effective stress for the graded FGC with $V_c^+ = 1.0$, $V_c^- = 0$ and $n = 2$.

For the condition (b) the resulting thermal stresses σ_{22} and σ_θ are in an opposite sense from those for condition (a). Figure 12 exhibits the contour of the normalized effective stress $\bar{\sigma}_e$ in the plate for $n = 2$ calculated with and without the temperature dependence on the material properties. The maximum effective stress is present at the middle points of the outer edges for the case of temperature-dependent material properties, but at the intersections between the surface of the hole and the x_1- and x_2-axis for

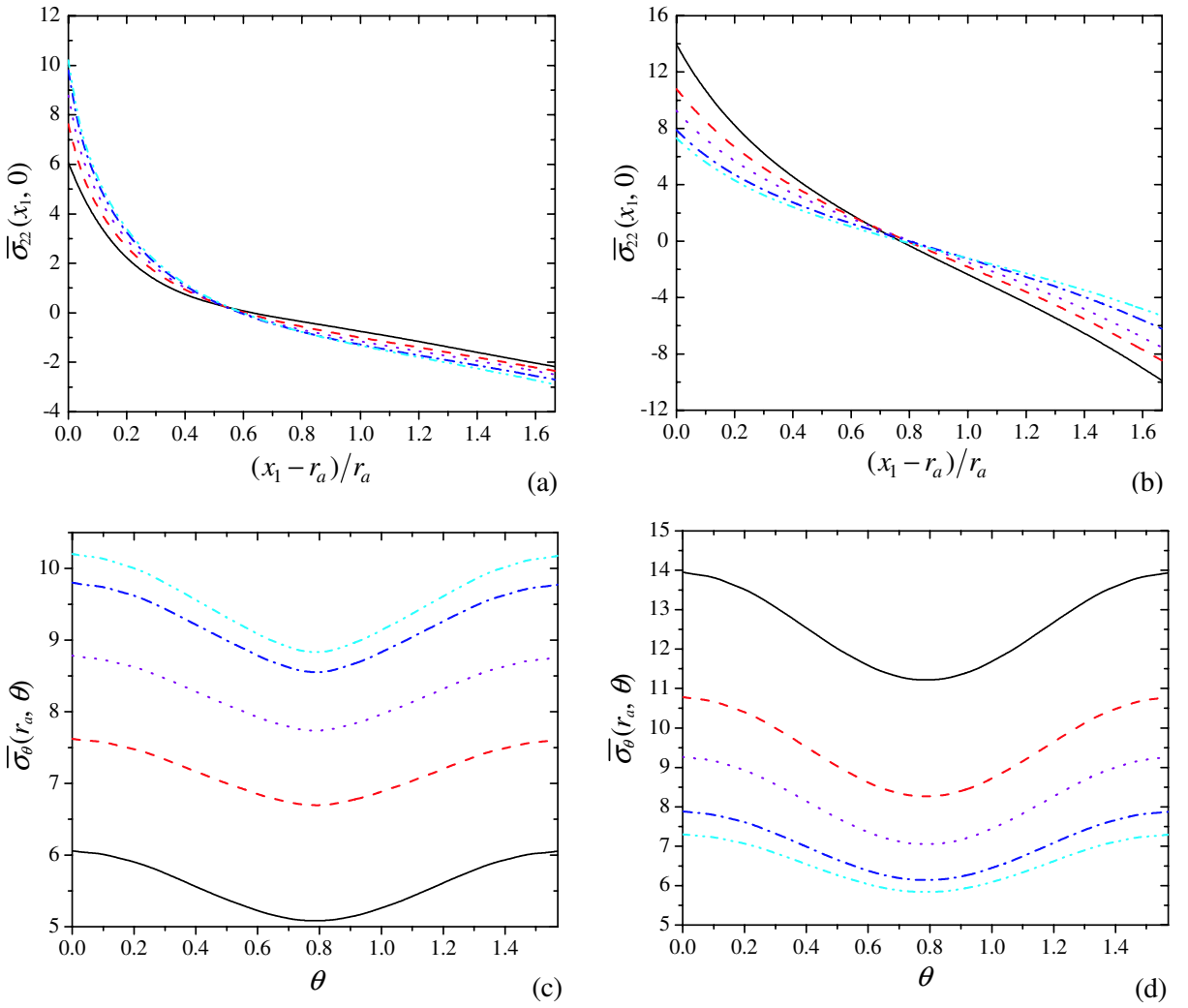

Figure 10. Variations of σ_{22} along the x_1-axis and hoop stress along the surface of the hole for different values of n with $V_c^+ = 1$ and $V_c^- = 0$. Left: temperature-dependent material properties; right: constant material properties. The temperature load is applied on the outer boundary.

the case of the constant material properties. The difference of the maximum $\bar{\sigma}_e$ calculated with the two sets of the material properties is much larger for condition (b) than for condition (a).

6. Conclusions

Due to the complex features of material nonhomogeneity in FGC materials and the temperature dependence on material properties it is almost impossible to obtain an exact solution for the thermomechanical response. In this work we have analyzed the thermomechanical deformation in the 2-D ZrO_2 and Ti-6Al-4V FGCs under elevated temperature loading using the mesh-free MLPG particle method. Both the rule

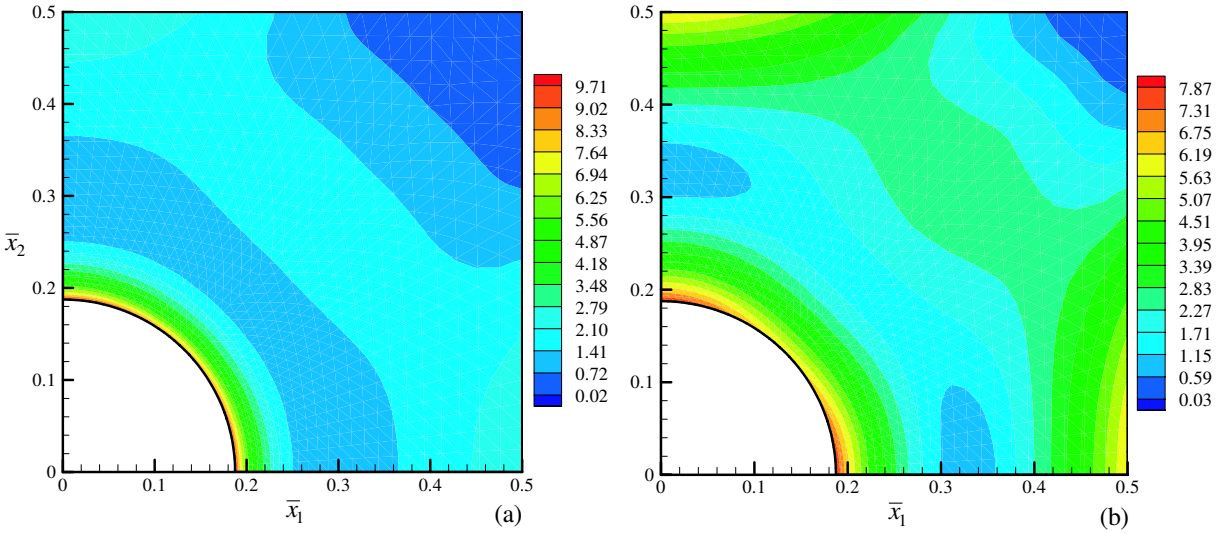

Figure 11. Normalized effective stress contours in the plate with $V_c^+ = 1$, $V_c^- = 0$, and $n = 2$ computed with (a) temperature-dependent material properties and (b) constant material properties; the temperature load is applied on the outer boundary.

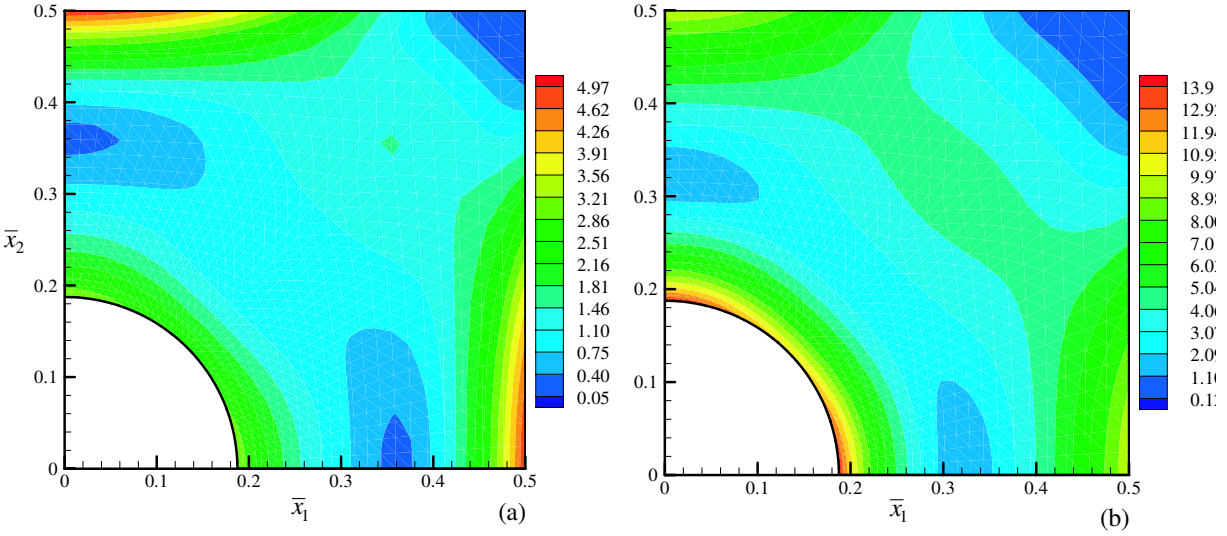

Figure 12. Normalized effective stress contours in the plate with $V_c^+ = 0$, $V_c^- = 1$, and $n = 2$ computed with (a) temperature-dependent material properties and (b) constant material properties; the temperature load is applied on the inner surface of the hole.

of mixtures and the micromechanical models are adopted to evaluate the effective material properties. Three illustrated examples, including a hollow cylinder, a clamped-clamped thick beam, and a square plate with a central hole, are presented. The numerical results show that the deformation and thermal stresses in an FGC computed temperature-dependent material properties are quite different than those

predicted with the constant material properties. Therefore, analyses that fail to consider the temperature dependence of material properties could result in a considerable error in thermomechanical response for an FGC in elevated temperature environments. More importantly, the FGC may not perform as initially expected if it is graded based on the constant material properties.

To accurately predict the thermomechanical responses for nonhomogeneous FGCs a high fidelity numerical tool is essential. Unlike the finite element method, the MLPG method requires only a set of nodes for both the interpolation of the trial functions and the integration of the weak forms. Besides, this method dictates the continuous material properties of FGMs directly to a quadrature point. These prominent features make the MLPG method well suited in the analysis of functionally graded composite structures.

References

[Atluri 2005] S. N. Atluri, *The meshless method (MLPG) for domain and BIE discretizations*, Tech Science Press, Los Angeles, 2005.

[Atluri and Zhu 1998] S. N. Atluri and T. Zhu, "A new meshless local Petrov–Galerkin (MLPG) approach in computational mechanics", *Comput. Mech.* **22**:2 (1998), 117–127.

[Chati and Mukherjee 2000] M. K. Chati and S. Mukherjee, "The boundary node method for three-dimensional problems in potential theory", *Int. J. Numer. Methods Eng.* **47**:9 (2000), 1523–1547.

[Ching and Chen 2006] H. K. Ching and J. K. Chen, "Thermomechanical analysis of functionally graded composites under laser heating by the MLPG method", *Comput. Model. Eng. Sci.* **13**:3 (2006), 199–218.

[Ching and Yen 2005] H. K. Ching and S. C. Yen, "Meshless local Petrov–Galerkin analysis for 2-D functionally graded elastic solids under mechanical and thermal loads", *Compos. B Eng.* **36**:3 (2005), 223–240.

[Christensen 1979] R. M. Christensen, *Mechanics of composite materials*, Wiley, New York, 1979.

[Cook et al. 1989] R. D. Cook, D. S. Malkus, and M. E. Plesha, *Concepts and applications of finite element analysis*, 3rd ed., Wiley, 1989.

[Dole and Hunter Jr. 1983] S. L. Dole and O. Hunter Jr., "Elastic properties of hafnium and zirconium oxides stabilized with praseodymium or terbium oxide", *J. Am. Ceram. Soc.* **66**:3 (1983), C–47–C–49.

[Hatta and Taya 1985] H. Hatta and M. Taya, "Effective thermal conductivity of a misoriented short fiber composite", *J. Appl. Phys.* **58**:7 (1985), 2478–2486.

[Mori and Tanaka 1973] T. Mori and K. Tanaka, "Average stress in matrix and average elastic energy of materials with misfitting inclusions", *Acta Metall.* **21**:5 (1973), 571–574.

[Ootao and Tanigawa 2004] Y. Ootao and Y. Tanigawa, "Transient thermoelastic problem of functionally graded thick strip due to nonuniform heat supply", *Compos. Struct.* **63**:2 (2004), 139–146.

[Ootao and Tanigawa 2005] Y. Ootao and Y. Tanigawa, "Three-dimensional solution for transient thermal stresses of functionally graded rectangular plate due to nonuniform heat supply", *Int. J. Mech. Sci.* **47**:11 (2005), 1769–1788.

[Praveen et al. 1999] G. N. Praveen, C. D. Chin, and J. N. Reddy, "Thermoelastic analysis of functionally graded ceramic-metal cylinder", *J. Eng. Mech.* **125**:11 (1999), 1259–1267.

[Qian and Batra 2004] L. F. Qian and R. C. Batra, "Transient thermoelastic deformations of a thick functionally graded plate", *J. Therm. Stresses* **27**:8 (2004), 705–740.

[Qian and Batra 2005] L. F. Qian and R. C. Batra, "Three-dimensional transient heat conduction in a functionally graded thick plate with a higher-order plate theory and a meshless local Petrov–Galerkin method", *Comput. Mech.* **35**:3 (2005), 214–226.

[Qian and Ching 2004] L. F. Qian and H. K. Ching, "Static and dynamic analysis of 2-D functionally graded elasticity by using meshless local Petrov–Galerkon method", *J. Chin. Inst. Eng.* **27** (2004), 491–503.

[Reddy and Chin 1998] J. N. Reddy and C. D. Chin, "Thermomechanical analysis of functionally graded cylinders and plates", *J. Therm. Stresses* **21** (1998), 593–626.

[Rosen and Hashin 1970] B. W. Rosen and Z. Hashin, "Effective thermal expansion coefficients and specific heats of composite materials", *Int. J. Eng. Sci.* **8**:2 (1970), 157–173.

[Sankar and Tzeng 2002] B. V. Sankar and J. T. Tzeng, "Thermal stresses in functionally graded beams", *AIAA J.* **40**:6 (2002), 1228–1232.

[Sladek et al. 2003] J. Sladek, V. Sladek, and C. Zhang, "Application of meshless local Petrov–Galerkin (MLPG) method to elastodynamic problems in continuously nonhomogeneous solids", *Comput. Model. Eng. Sci.* **4**:6 (2003), 637–647.

[Sladek et al. 2005] J. Sladek, V. Sladek, J. Krivacek, and C. Zhang, "Meshless local Petrov–Galerkin method for stress and crack analysis in 3-D axisymmetric FGM bodies", *Comput. Model. Eng. Sci.* **8**:3 (2005), 259–270.

[Takahashi et al. 1992] H. Takahashi, T. Ishikawa, D. Okugawa, and T. Hashida, "Laser and plasma-arc thermal shock fatigue evaluation procedure for functionally graded materials", pp. 543–554 NATO ASI Series E: Appl. Sci. **241**, 1992.

[Tanigawa et al. 1997] Y. Tanigawa, M. Matsumoto, and T. Ahai, "Optimization of material composition to minimize thermal stresses in nonhomogeneous plate subjected to unsteady heat supply", *JSME Int. J. Ser. A Solid Mech. Mater. Eng.* **40** (1997), 84–93.

[Tarn 2001] J. Q. Tarn, "Exact solutions for functionally graded anisotropic cylinders subjected to thermal and mechanical loads", *Int. J. Solids Struct.* **38**:46-47 (2001), 8189–8206.

[Vel and Batra 2002] S. S. Vel and R. C. Batra, "Exact solution for thermoelastic deformations of functionally graded thick rectangular plates", *AIAA J.* **40**:7 (2002), 1421–1433.

[Vel and Batra 2003] S. S. Vel and R. C. Batra, "Three-dimensional analysis of transient thermal stresses in functionally graded plates", *Int. J. Solids Struct.* **40**:25 (2003), 7181–7196.

[Wang and Mai 2005] B. L. Wang and Y. W. Mai, "Transient one-dimensional heat conduction problems solved by finite element", *Int. J. Mech. Sci.* **47**:2 (2005), 303–317.

[Wang and Tian 2005] B. L. Wang and Z. H. Tian, "Application of finite element–finite difference method to the determination of transient temperature field in functionally graded materials", *Finite Elem. Anal. Des.* **41**:4 (2005), 335–349.

[Zhu and Atluri 1998] T. Zhu and S. N. Atluri, "A modified collocation method and a penalty formulation for enforcing the essential boundary conditions in the element free Galerkin method", *Comput. Mech.* **21**:3 (1998), 211–222.

[Zimmerman and Lutz 1999] R. W. Zimmerman and M. P. Lutz, "Thermal stresses and thermal expansion in a uniformly heated functionally graded cylinder", *J. Therm. Stresses* **22**:2 (1999), 177–188.

Received 9 Sep 2006. Accepted 29 Nov 2006.

H. K. CHING: *Department of Mechanical and Aerospace Engineering, University of Missouri, Columbia, MO 65201, United States*

J. K. CHEN: ChenJnK@missouri.edu
Department of Mechanical and Aerospace Engineering, University of Missouri, Columbia, MO 65201, United States